

## Raman mapping of photodissociation regions in Orion

WILLIAM J. HENNEY<sup>1</sup>

<sup>1</sup>*Instituto de Radioastronomía y Astrofísica, Universidad Nacional Autónoma de México, Apartado Postal 3-72, 58090 Morelia, Michoacán, Mexico*

### Abstract

I show that the broad Raman-scattered wings of H $\alpha$  can be used to map neutral gas illuminated by high-mass stars in star forming regions. The near wings ( $\Delta\lambda \approx \pm 10$  Å) trace neutral hydrogen columns of about  $5 \times 10^{20}$  cm $^{-2}$ , while the farther wings ( $|\Delta\lambda| > 30$  Å) trace columns of about  $5 \times 10^{21}$  cm $^{-2}$ . Absorption features in the pseudo-continuum at 6633 and 6664 Å correspond to neutral oxygen far-ultraviolet absorption lines at 1027.43 Å and 1028.16 Å.

**Keywords:** Atomic physics; Radiative transfer; Photodissociation regions

### 1. INTRODUCTION

Raman scattering is the inelastic analog of Rayleigh scattering by atoms or molecules. Both processes begin with a radiation-induced transition of an electron to a virtual bound state (non-eigenstate). In Rayleigh scattering, the electron returns to its original state, resulting in the radiation being re-emitted with its original frequency (elastic scattering). In Raman scattering, on the other hand, the electron undergoes a transition to a different excited state, resulting in radiation being re-emitted at a much lower frequency. Recently, Dopita et al. (2016) identified exceedingly broad wings to the H $\alpha$  6563 Å line in the Orion Nebula and a number of H $\text{II}$  regions in the Magellanic Clouds, which they ascribe to Raman scattering of ultraviolet radiation in the vicinity of the Ly $\beta$  1025 Å transition. Raman scattering in astrophysical sources was first identified in symbiotic stars (Schmid 1989), where FUV O VI emission lines at 1032 and 1038 Å produce broad emission features at 6827 and 7088 Å. This illustrates a curious feature of Raman scattering (Nussbaumer et al. 1989): the relative width  $\Delta\lambda/\lambda$  of spectral features is amplified by a factor  $\lambda(\text{H}\alpha)/\lambda(\text{Ly}\beta) \approx 6.4$  when passing from the FUV to the optical domain.

Dopita et al. (2016) propose that the Raman wings form at the transition zone near the ionization fronts in H $\text{II}$  regions. However, the total neutral hydrogen column through the ionization front can be no more than about  $10/\sigma_0 \approx 2 \times 10^{18}$  cm $^{-2}$ , where  $\sigma_0 \approx 6.3 \times 10^{-18}$  cm $^2$  is the ground-state hydrogen photoionization cross section at threshold (Osterbrock & Ferland 2006). The Raman scattering cross section at wavelengths responsible for the observed wings is much lower than this:  $\sigma_{\text{Raman}} \sim 10^{-21}$  cm $^2$  (Chang et al. 2015), meaning that the Raman scattering optical depth through the ionization front is only of order 0.001. A vastly larger column density of neutral hydrogen ( $\approx 10^{21}$  cm $^{-2}$ ) is available in the photodissociation region (PDR) outside the ionization front, so it is more likely that Raman scattering will occur there instead, so long as there is sufficient far ultraviolet radiative flux.

This paper is organized as follows. § 2 recapitulates the basic theory of Raman scattering, concentrating on the wavelength transformation from the FUV domain around Ly $\beta$  to optical domain around H $\alpha$ . In addition, polynomial fits are provided to the wavelength dependence of the total (Rayleigh plus Raman) scattering cross section and the Raman H $\alpha$  branching ratio. § 3 then presents archival VLT-MUSE integral field spectroscopy of the Orion Nebula, which allows the broad H $\alpha$  wings to be spatially mapped in unprecedented detail and compared with other tracers of ionized and neutral zones in the nebula. Two components of the O I UV resonance multiplet  $2p^4\ ^3P \rightarrow 3d\ ^3D^0$  are detected as absorption features at 6633 and 6664 Å against the H $\alpha$  Raman wings. § 4 presents archival Keck-HIRES slit spectroscopy, which shows the profile of the 6664 Å absorption line with an effective velocity resolution of 1 km s $^{-1}$ . § 5 discusses the implications of these results for the structure and dynamics of the PDRs in Orion, together with the prospects for using Raman spectral mapping as a diagnostic tool in the study of other high-mass star formation regions.

### 2. RAMAN SCATTERING THEORY

When a photon is Raman-scattered from the vicinity of Ly $\beta$  (UV domain) to the vicinity of H $\alpha$  (optical domain) its wavelength is transformed from  $\lambda_1$  to  $\lambda_2$ . Intervals in frequency ( $\nu = c/\lambda$ ) or wavenumber ( $\tilde{\nu} = 1/\lambda$ ) space are conserved between the two

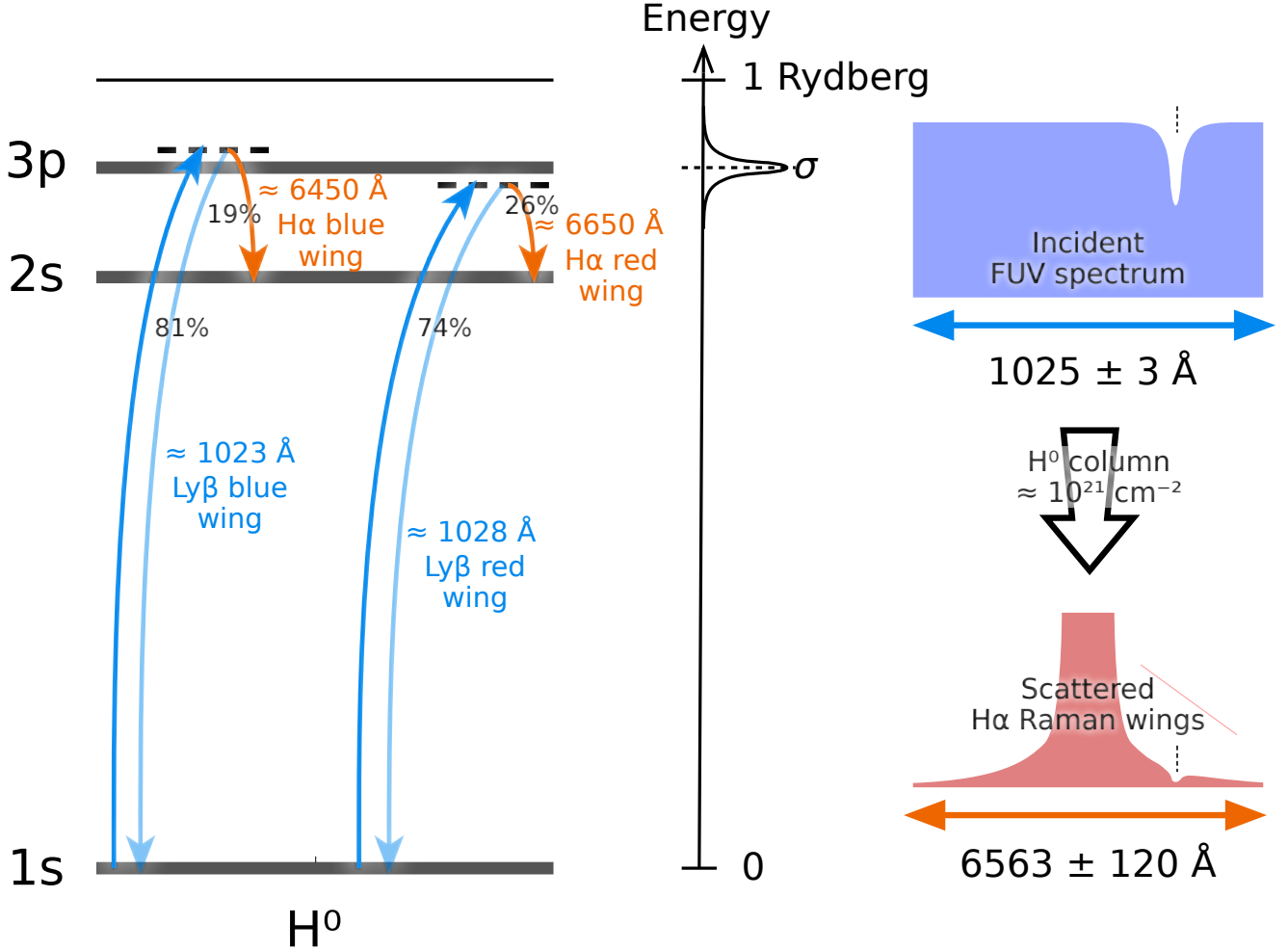


**Figure 1.** Schematic illustration of Raman scattering of photons from the Ly $\beta$  wings to the H $\alpha$  wings. The relevant energy levels of neutral hydrogen are shown at left. Far ultraviolet photons that are shifted by about  $\Delta\lambda_1 = \pm 1$  to 3  $\text{\AA}$  from the Ly $\beta$  rest wavelength can excite transitions from the ground 1s level to a virtual state adjacent to 3p. Most such excitations decay back to 1s (Rayleigh scattering), but in about one-fifth of cases the decay is to 2s instead (Raman scattering). The scattering cross section falls approximately as  $\Delta\lambda_1^{-2}$ , which gives broad Lorentzian wings to the H $\alpha$  line, as shown at right. A bandwidth of  $\Delta\lambda_1 = \pm 3 \text{ \AA}$  around Ly $\beta$  is transformed to a bandwidth  $\Delta\lambda_2 = \pm 120 \text{ \AA}$  around H $\alpha$ . A narrow absorption line in the incident FUV spectrum (vertical thin dashed line) becomes a much broader notch in the scattered wings.

domains. For example the wavenumber displacement from the H $\alpha$  line center can be written in two ways:

$$\Delta\tilde{\nu} = \tilde{\nu}_1 - \tilde{\nu}(\text{Ly}\beta) = \tilde{\nu}_2 - \tilde{\nu}(\text{H}\alpha), \quad (1)$$

from which it follows that

$$\lambda_2 = \left( \frac{1}{\lambda(\text{H}\alpha)} + \frac{1}{\lambda_1} - \frac{1}{\lambda(\text{Ly}\beta)} \right)^{-1}. \quad (2)$$

The wavelengths  $\lambda(\text{Ly}\beta)$  and  $\lambda(\text{H}\alpha)$ , together with their corresponding wavenumbers, are given in Table 1 (all wavelengths are on the vacuum scale unless otherwise noted). For both lines, a weighted average over the  $3p\ ^2P_{1/2}$  and  $3p\ ^2P_{3/2}$  upper levels is used, assumed to be populated according to their statistical weights, with individual component wavelengths obtained from Tab. XXVIII of Mohr et al. (2008). Note that the electric dipole selection rules mean that only  $3p \rightarrow 2s$  transitions contribute to H $\alpha$  in the Raman scattering context. The wavelength is therefore slightly shorter than the value obtained for the H $\alpha$  recombination

**Table 1.** FUV/optical wavelength equivalencies for Raman scattering

Ion	Transition	$J_i \rightarrow J_k$	$\lambda_1, \text{\AA}$	$\tilde{\nu}_1, \text{cm}^{-1}$	$\Delta\tilde{\nu}, \text{cm}^{-1}$	$\tilde{\nu}_2, \text{cm}^{-1}$	$\lambda_2, \text{\AA}$	$\lambda_{\text{air}}, \text{\AA}$
			.... Ly $\beta$ , $n = 1$ ....			.....	H $\alpha$ , $n = 2$	.....
H I	$ns^2 \text{S} \rightarrow 3p^2 \text{P}$	$\frac{1}{2} \rightarrow \frac{1}{2}, \frac{3}{2}$	1025.72220	97492.283	0.000	15233.329	6564.553	6562.740
O I	$2s^2 2p^4 \text{P} \rightarrow 2s^2 2p^3(^4\text{S})3d \text{D}^o$	0 → 1	1028.15729	97261.383	-230.900	15002.429	6665.587	6663.747
		1 → 1	1027.43139	97330.100	-162.183	15071.146	6635.196	6633.364
		1 → 2	1027.43077	97330.159	-162.124	15071.205	6635.170	6633.338
		2 → 1	1025.76339	97488.369	-3.914	15229.415	6566.240	6564.427
		2 → 2	1025.76276	97488.429	-3.854	15229.475	6566.215	6564.401
		2 → 3	1025.76170	97488.530	-3.753	15229.576	6566.171	6564.358
Si II	$3s^2 3p^2 \text{P}^o \rightarrow 3s^2 5s \text{S}$	$\frac{1}{2} \rightarrow \frac{1}{2}$	1020.6989	97972.086	+479.803	15713.132	6364.104	6362.345
		$\frac{1}{2} \rightarrow \frac{3}{2}$	1023.7001	97684.859	192.576	15425.905	6482.602	6480.811

line, which includes additional contributions from  $3s \rightarrow 2p$  and  $3d \rightarrow 2p$ . The shift is of order  $-0.05 \text{\AA}$  or  $-2 \text{ km s}^{-1}$  with respect to the Case B results reported in Tab. 6a of Clegg et al. (1999).

Also listed in Table 1 are the Raman transformations  $\lambda_1 \rightarrow \lambda_2$  for the rest wavelengths of transitions between the ground  $2s^2 2p^4 \text{P}$  term of neutral  $^{16}\text{O}$  and the excited  $2s^2 2p^3 3d \text{D}^o$  term. The O I data is obtained from highly accurate laser metrology (Ivanov et al. 2008; Marinov et al. 2017), with a precision of  $0.08 \text{ cm}^{-1}$  or better. The fine structure splitting between the  $J_k$  levels of the excited term ( $\sim 0.1 \text{ cm}^{-1}$ ) is much smaller than that between the  $J_i$  levels of the ground term ( $\sim 100 \text{ cm}^{-2}$ ), so that the 6 transitions fall into 3 well-separated groups. The three transitions from the lowest energy  $J_i = 2$  level are very close to Ly $\beta$  ( $\Delta\tilde{\nu} \approx 4 \text{ cm}^{-1}$ ), whereas the two transitions from  $J_i = 1$  ( $\Delta\tilde{\nu} \approx 162 \text{ cm}^{-1}$ ) and the single transition from  $J_i = 0$  ( $\Delta\tilde{\nu} \approx 231 \text{ cm}^{-1}$ ) lie increasingly to the red. The corresponding wavelengths in the optical domain,  $\lambda_2$ , are therefore on the red side of H $\alpha$ . The final column of the table uses STP refractive indices (Greisen et al. 2006) to convert  $\lambda_2$  to air wavelengths,  $\lambda_{\text{air}}$ , for ease of comparison with ground-based optical spectroscopy. The resultant wavelength is  $6663.747 \text{\AA}$  for the line from  $J_i = 0$ , with an uncertainty of about  $0.004 \text{\AA}$ , which is much smaller than typical observational precision (for instance,  $0.07 \text{\AA}$  for a very high resolution spectrograph with resolving power of  $R = 10^5$ ). The two lines from  $J_i = 1$ , with a separation of  $0.028 \text{\AA}$ , will always be blended in observations, giving a mean wavelength of  $6633.347 \text{\AA}$  (assuming the upper levels are distributed according to statistical weight  $2J_k + 1$ ). Similarly, the three lines from  $J_i = 2$  have a mean wavelength of  $6564.386 \text{\AA}$ , but this is so close to H $\alpha$  (corresponding to a Doppler shift of  $+75 \text{ km s}^{-1}$ ) that it would be very difficult to observe.

The total cross-section for the off-resonance  $1s \rightarrow 3p$  transition in  $\text{H}^0$  is calculated in § 2 of Chang et al. (2015) from second order time-dependent perturbation theory. Results are presented in the upper panel of Figure 1 of that paper in terms of a Doppler velocity factor  $\Delta V_1$ , which in the notation of the current paper is

$$\Delta V_1 = c \left( \frac{\lambda_1}{\lambda(\text{Ly}\beta)} - 1 \right). \quad (3)$$

The observed Raman-scattered wings of H $\alpha$  that are analyzed below are typically within  $\Delta\lambda_2 \sim \pm 100 \text{\AA}$  of the line core. It is therefore convenient to define a dimensionless wavelength in the optical domain as

$$x = \frac{\lambda_2 - \lambda(\text{H}\alpha)}{100 \text{\AA}}, \quad (4)$$

which corresponds to  $x \approx \Delta V_1 / 714 \text{ km s}^{-1}$  in the FUV domain. The total cross section in the range  $0.4 < |x| < 2.3$  can then be fit as follows:

$$\frac{\sigma}{10^{-21} \text{ cm}^2} = \begin{cases} 0.2186x^{-2} - 0.0344x^{-1} - 0.0054 & \text{if } x < 0 \\ 0.2367x^{-2} - 0.0187x^{-1} + 0.0041 & \text{if } x > 0 \end{cases} \quad (5)$$

Note that separate fits are given for the blue ( $x < 0$ ) and red ( $x > 0$ ) wings of H $\alpha$  since the cross section, although approximately Lorentzian, is not exactly symmetric, being stronger on the blue side (by about 10% for  $x = \pm 1$ ).

The fraction of all  $1s \rightarrow 3p$  excitations that result in Raman scattering to an optical photon is given by the branching ratio,  $f_{\text{H}\alpha}$ , with the remaining fraction,  $1 - f_{\text{H}\alpha}$ , resulting in elastic Rayleigh scattering in which the photon remains in the FUV domain.

**Table 2.** Wavelength bands used for Raman wing extraction

	Band	$\langle \Delta\lambda_2 \rangle, \text{\AA}$	$\lambda_{\min}, \text{\AA}$	$\lambda_{\max}, \text{\AA}$	$f_{\text{H}\alpha}$	$\langle \sigma_\lambda \rangle, 10^{-21} \text{ cm}^2$	Contamination
Blue wing	B133	-132.8	6414.85	6445.45	0.180	0.144	
	B080	-79.5	6469.25	6496.45	0.196	0.378	Sky 6471, 6478
	B054	-53.6	6499.85	6517.70	0.205	0.802	O II? 6502, 6510, Sky 6507
	B033	-32.8	6518.55	6540.65	0.212	2.069	[N II] 6527.24, [Ni III] 6533.76
Red wing	R040	40.3	6594.20	6611.20	0.238	1.451	Sky 6603
	R058	57.7	6612.05	6628.20	0.244	0.695	
	R087	87.1	6638.40	6660.50	0.255	0.299	[Cr IV]? 6641
	R136	135.7	6688.55	6708.95	0.274	0.119	He I 6699

**Table 3.** Fit parameters from Gaussian line fits

Region	OI			Ni II		
	A	V	$\sigma$	A	V	$\sigma$
A						
B						
C						
D						
E						

The results for  $f_{\text{H}\alpha}$  are also shown in Figure 1 of Chang et al. (2015) and can be fit as follows in the range  $|x| < 5$ :

$$f_{\text{H}\alpha} = 0.2238 + 0.0363x + 0.0024x^2. \quad (6)$$

The relative accuracy of all these fits is better than 1% within the stated range (corresponding to  $\sigma \approx 10^{-22} \text{ cm}^2$  to  $10^{-21} \text{ cm}^2$ ), which is perfectly adequate for the purposes of this paper. Note that the branching ratio increases with  $x$ , which means that the product  $\sigma f_{\text{H}\alpha}$  is stronger on the red side of H $\alpha$ .

### 3. SPECTRAL MAPPING OF RAMAN WINGS

The 6633 Å and 6664 Å lines are clearly detected in the MUSE spectra as absorption features against the pseudo-continuum of the broad H $\alpha$  wings (see Fig XX), although the latter is blended with a Ni II emission line at 6666.8 Å. This is further proof of the Raman scattering nature of the wings.

MUSE (Bacon et al. 2010) observations of the Orion Nebula (Weilbacher et al. 2015; Mc Leod et al. 2015).

The bands are chosen to avoid the stronger sky lines (e.g., 6498 Å) and nebula lines (e.g., ), but some weak line contamination remains, as listed in the last column of Table 2.

The 21 cm H I line (van der Werf et al. 2013) probes deeper zones of the PDR than the Raman scattering, since it peaks at the position of the H<sub>2</sub> emission.

### 4. HIGH-RESOLUTION SPECTROSCOPY OF RAMAN-SCATTERED O I 1028 Å

Keck HIRES spectra described in Henney & O'Dell (1999) and Bally et al. (2000). The spectrum I use is of HH 529 base region in Orion South. Published results from these data have concentrated on strong nebular lines, but here I use a small section of the spectrum in the range 6660 Å to 6670 Å for reasons which will become apparent.

### 5. DISCUSSION

Location of H<sup>0</sup>. Neutral veil in front of nebula has column density of  $1.6 \times 10^{21} \text{ cm}^{-2}$  and  $3.2 \times 10^{21} \text{ cm}^{-2}$  in components A and B (Abel et al. 2006).

#### 5.1. Structure of the Orion Bar

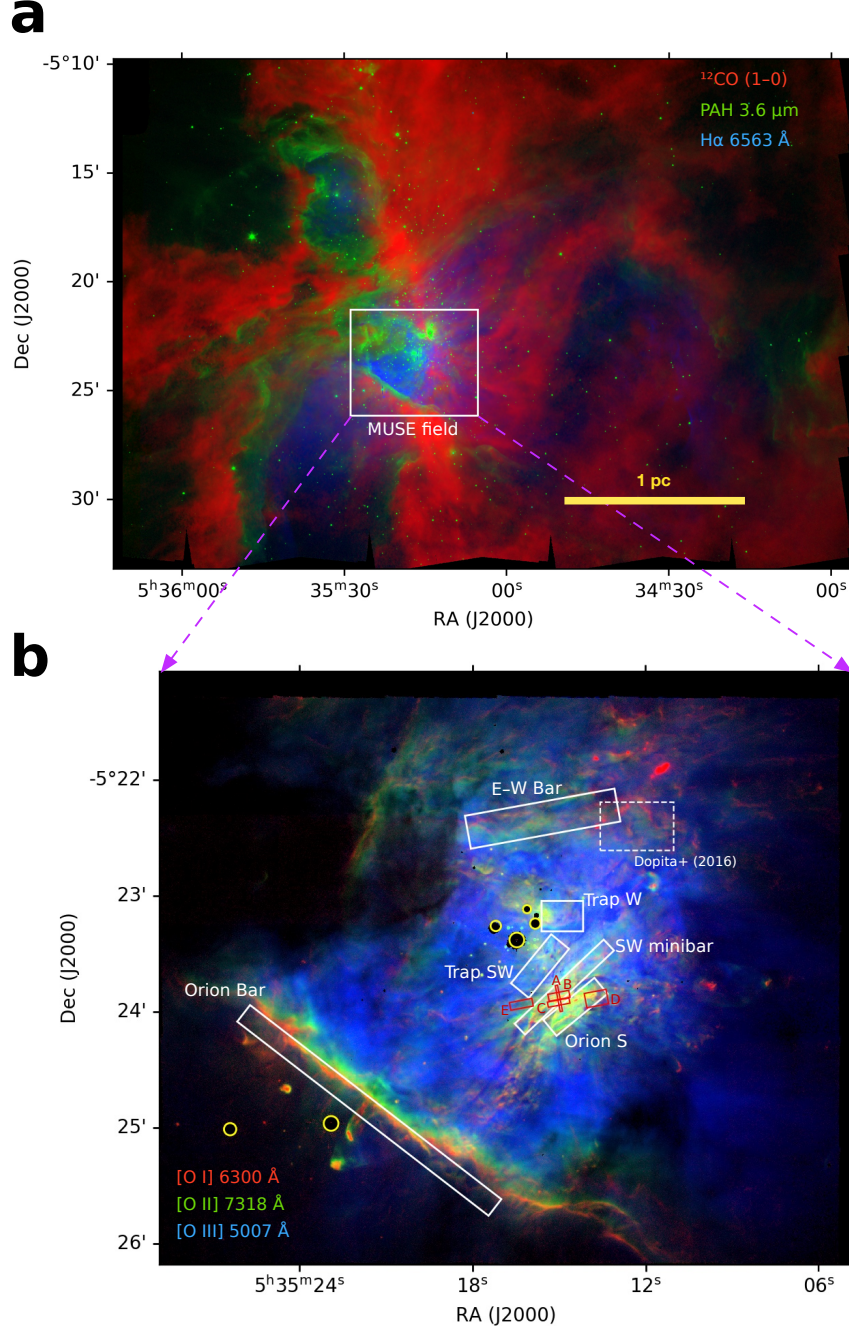


**Figure 2.** (a) Panoramic view of the Orion Nebula region on parsec scales. Red channel of background image shows  $^{12}\text{CO}$  emission from dense molecular gas (Carma-NRO Orion Survey, Kong et al. 2018). Green channel shows near-infrared continuum from PAH grains in neutral gas (Spitzer Orion Survey, Megeath et al. 2012). Blue channel shows optical H $\alpha$  emission from ionized gas (WFI camera on ESO 2.2 m La Silla, Da Rio et al. 2009). The white box shows the field of view observed with MUSE. (b) Locations within the nebula of the extraction regions for the MUSE spectra shown in Figure 3 (white boxes) and the Keck HIRES spectra shown in Figure 7 (red boxes). The region of the spectrum obtained in Dopita et al. (2016) is shown by the dashed box. Background image shows oxygen emission lines extracted from the MUSE data cube: [O I]  $\lambda 6300$  Å (red channel), which traces ionization fronts and shocks in neutral gas; [O II]  $\lambda 7318$  Å (green channel), which traces the outer layers of the photoionized nebula; and [O III]  $\lambda 5007$  Å (blue channel), which traces the highly ionized interior of the nebula.

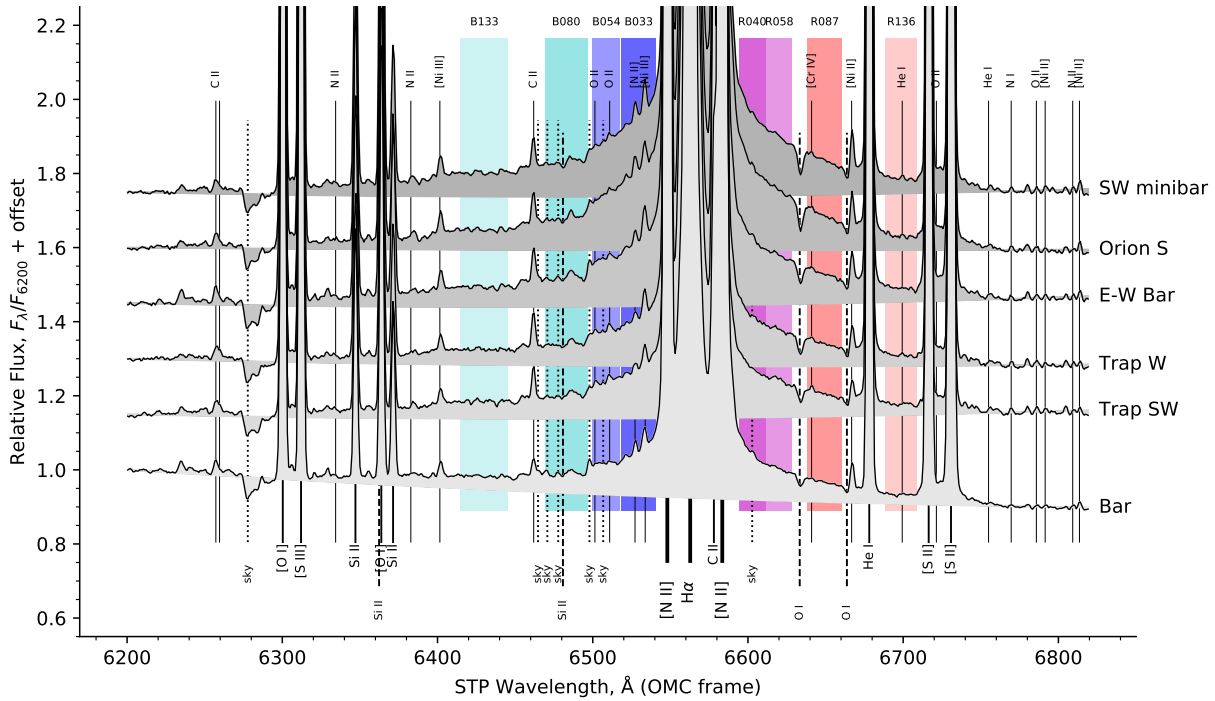


**Figure 3.** MUSE spectra centered on the H $\alpha$  line, showing the broad Raman-scattered wings.

Geometry of bar: in [Henney et al. \(2005\)](#) I pointed out that a diverging cylindrical geometry is necessary to explain the sharp peak in the [N II] emissivity seen at the ionization front. It has been apparent since [O'Dell & Yusef-Zadeh \(2000\)](#) that the nebula contains many bar-like features.

[Salgado et al. \(2016\)](#) had found low dust cross-section in Orion Bar PDR, but there are loopholes. First, they assume plane-parallel geometry with exactly edge-on viewing angle, while in reality it is a roughly cylindrical filament. Second, they ignore scattering, see [Watson et al. \(1998\)](#). Also, density increase with depth

### 5.2. Miscellany

The effective resolving power of the optical spectrograph is multiplied by 6.4 for the FUV domain.

The O I lines should be in absorption in the spectrum seen by the Raman scatterers.

Non-equilibrium PDRs ([Stoerzer & Hollenbach 1998](#); [Bertoldi & Draine 1996](#)). Recent models from [Bron et al. \(2018\)](#).

C I emission from non-steady PDRs ([Stoerzer et al. 1997](#)) (fine structure lines, but maybe optical lines would be similar).

[Escalante et al. \(1991\)](#) model the far-red [C I] line as recombination of C<sup>+</sup>.

O VI 1037.62, 1031.93 absorption line in wind. No evidence for a blue absorption edge at  $V = 1200 \text{ km s}^{-1}$ , which would be at  $\lambda_2 = 6649 \text{ Å}$ , right in middle of R087 band.

Even for high PDR optical depth, no multiple Raman scattering will occur since the population of 2s is very small and the post-scattered photons have insufficient energy to excite any transitions from 1s.

### ACKNOWLEDGMENTS

This work has made use of the Atomic Line List<sup>1</sup> ([Van Hoof 2018](#)).

### REFERENCES

- Abel, N. P., Ferland, G. J., O'Dell, C. R., Shaw, G., & Troland, T. H. 2006, ApJ, 644, 344, doi: [10.1086/500819](https://doi.org/10.1086/500819)
- Bacon, R., Accardo, M., Adjali, L., et al. 2010, in Society of Photo-Optical Instrumentation Engineers (SPIE) Conference Series, Vol. 7735, Proc. SPIE, 773508, doi: [10.1117/12.856027](https://doi.org/10.1117/12.856027)

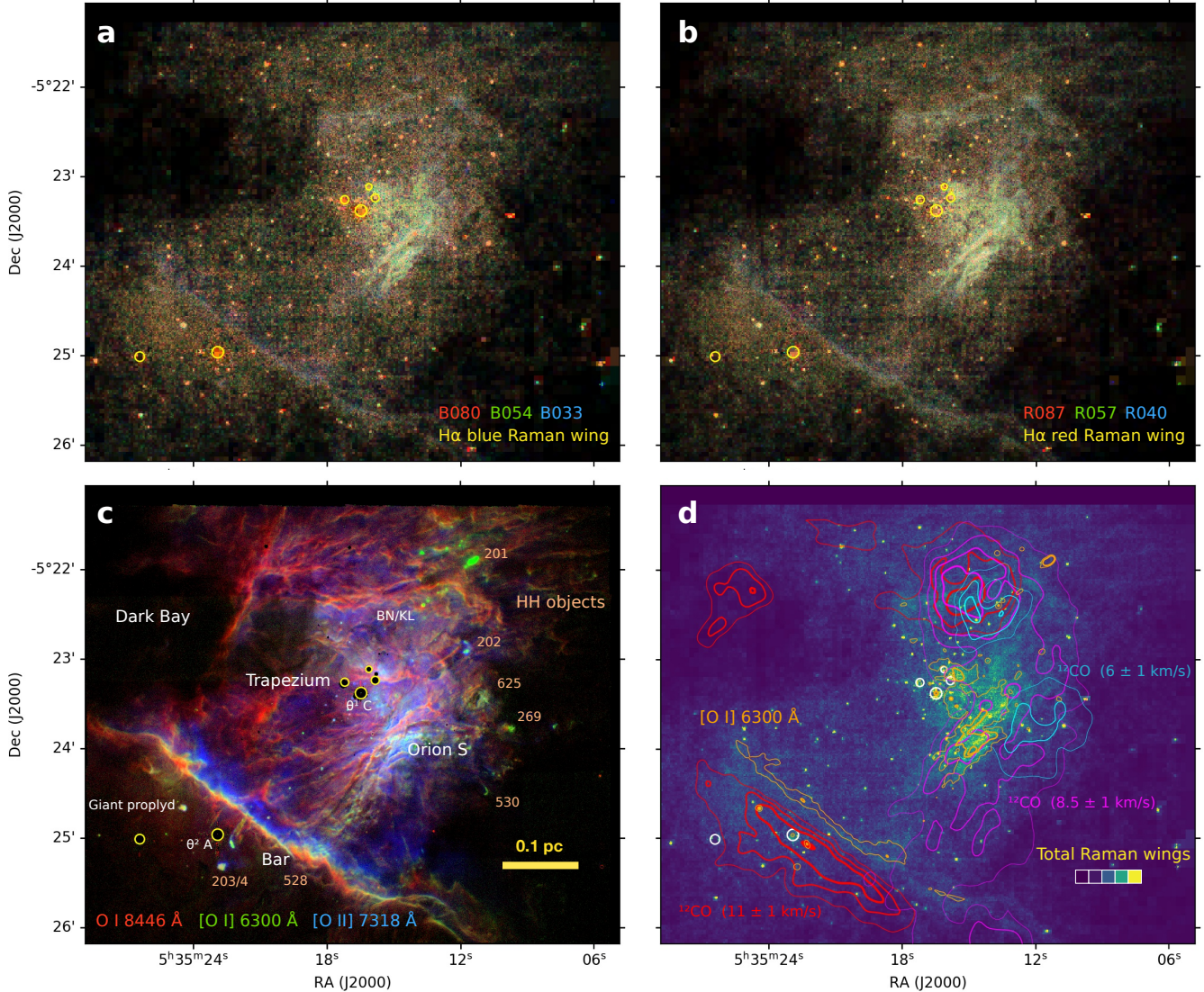


**Figure 4.** Spatial distribution of Raman-scattered wings in H $\alpha$

Bally, J., O'Dell, C. R., & McCaughrean, M. J. 2000, AJ, 119, 2919, doi: [10.1086/301385](https://doi.org/10.1086/301385)

Bertoldi, F., & Draine, B. T. 1996, ApJ, 458, 222, doi: [10.1086/176805](https://doi.org/10.1086/176805)

Bron, E., Agúndez, M., Goicoechea, J. R., & Cernicharo, J. 2018, arXiv e-prints. <https://arxiv.org/abs/1801.01547>

Chang, S.-J., Heo, J.-E., Di Mille, F., et al. 2015, ApJ, 814, 98, doi: [10.1088/0004-637X/814/2/98](https://doi.org/10.1088/0004-637X/814/2/98)

Clegg, R. E. S., Miller, S., Storey, P. J., & Kisielius, R. 1999, A&AS, 135, 359, doi: [10.1051/aa:1999178](https://doi.org/10.1051/aa:1999178)

Da Rio, N., Robberto, M., Soderblom, D. R., et al. 2009, ApJS, 183, 261, doi: [10.1088/0067-0049/183/2/261](https://doi.org/10.1088/0067-0049/183/2/261)

Dicker, S. R., Mason, B. S., Korngut, P. M., et al. 2009, ApJ, 705, 226, doi: [10.1088/0004-637X/705/1/226](https://doi.org/10.1088/0004-637X/705/1/226)

Dopita, M. A., Nicholls, D. C., Sutherland , R. S., Kewley, L. J., &

Groves, B. A. 2016, ApJL, 824, L13,

doi: [10.3847/2041-8205/824/1/L13](https://doi.org/10.3847/2041-8205/824/1/L13)

Escalante, V., Sternberg, A., & Dalgarno, A. 1991, ApJ, 375, 630, doi: [10.1086/170225](https://doi.org/10.1086/170225)

Foster, J. B., & Goodman, A. A. 2006, ApJL, 636, L105, doi: [10.1086/500131](https://doi.org/10.1086/500131)

Goicoechea, J. R., Pety, J., Cuadrado, S., et al. 2016, Nature, 537, 207, doi: [10.1038/nature18957](https://doi.org/10.1038/nature18957)

Green, D. A. 1991, MNRAS, 253, 350, doi: [10.1093/mnras/253.2.350](https://doi.org/10.1093/mnras/253.2.350)

Green, D. A., & Padman, R. 1993, MNRAS, 263, 535, doi: [10.1093/mnras/263.2.535](https://doi.org/10.1093/mnras/263.2.535)

Greisen, E. W., Calabretta, M. R., Valdes, F. G., & Allen, S. L. 2006, A&A, 446, 747, doi: [10.1051/0004-6361:20053818](https://doi.org/10.1051/0004-6361:20053818)

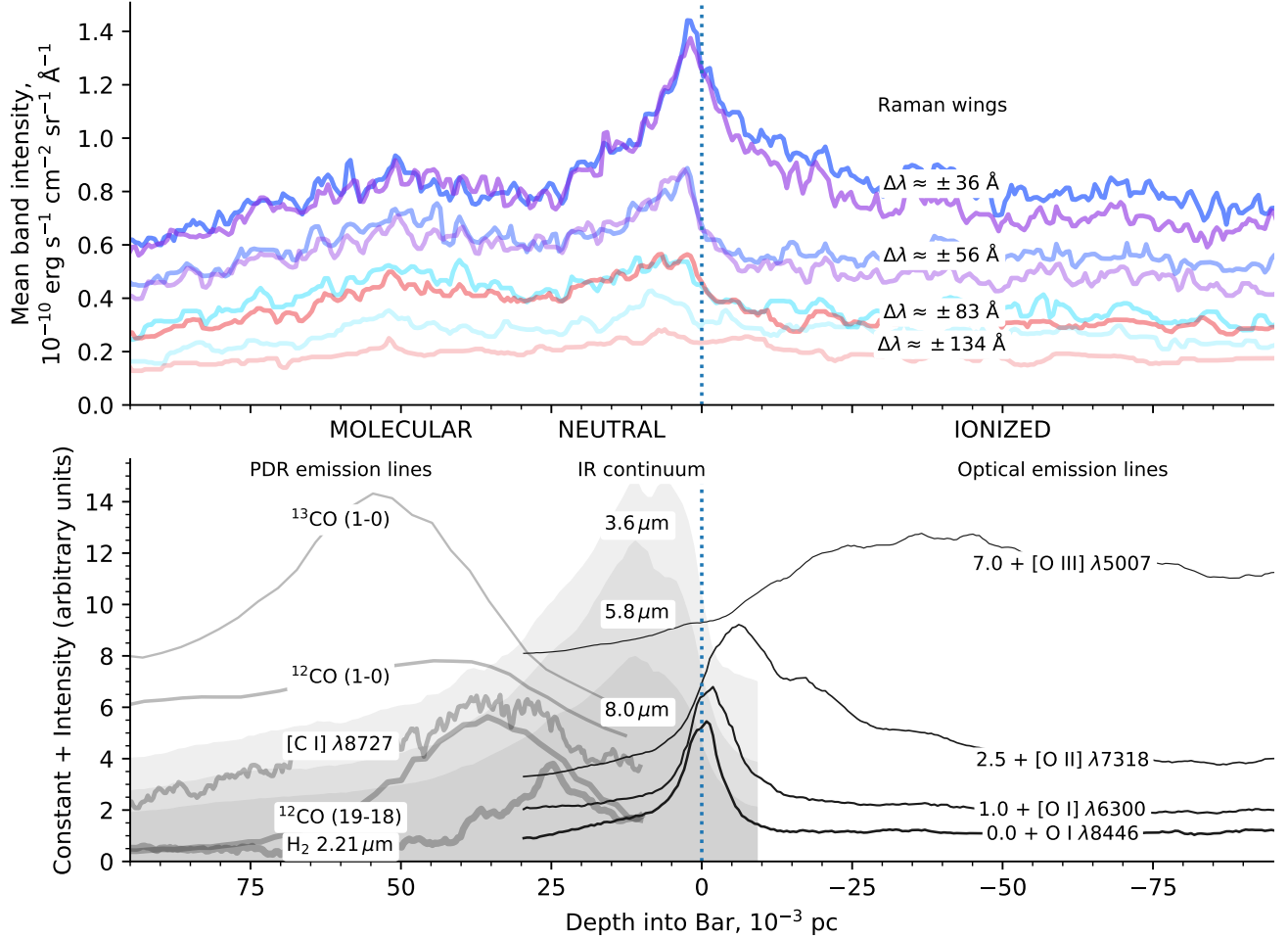


**Figure 5.** Spatial cut of Raman-scattered H $\alpha$  wing intensity across the Orion Bar (top panel). Matched red and blue wing bands are shown with color scheme matching Fig. 3.)

Henney, W. J., Arthur, S. J., Williams, R. J. R., & Ferland, G. J. 2005, ApJ, 621, 328, doi: [10.1086/427491](https://doi.org/10.1086/427491)

Henney, W. J., & O'Dell, C. R. 1999, AJ, 118, 2350, doi: [10.1086/301087](https://doi.org/10.1086/301087)

Ivanov, T. I., Salumbides, E. J., Vieitez, M. O., et al. 2008, MNRAS, 389, L4, doi: [10.1111/j.1745-3933.2008.00507.x](https://doi.org/10.1111/j.1745-3933.2008.00507.x)

Kissler-Patig, M., Pirard, J. F., Casali, M., et al. 2008, A&A, 491, 941, doi: [10.1051/0004-6361:200809910](https://doi.org/10.1051/0004-6361:200809910)

Kong, S., Arce, H. G., Feddersen, J. R., et al. 2018, ApJS, 236, 25, doi: [10.3847/1538-4365/aabafc](https://doi.org/10.3847/1538-4365/aabafc)

Marinov, D., Booth, J. P., Drag, C., & Blondel, C. 2017, Journal of Physics B Atomic Molecular Physics, 50, 065003, doi: [10.1088/1361-6455/aa5a88](https://doi.org/10.1088/1361-6455/aa5a88)

Mc Leod, A. F., Weilbacher, P. M., Ginsburg, A., et al. 2015, ArXiv e-prints. <https://arxiv.org/abs/1511.01914>

Megeath, S. T., Gutermuth, R., Muzerolle, J., et al. 2012, AJ, 144, 192, doi: [10.1088/0004-6256/144/6/192](https://doi.org/10.1088/0004-6256/144/6/192)

Mohr, P. J., Taylor, B. N., & Newell, D. B. 2008, Rev. Mod. Phys., 80, 633, doi: [10.1103/RevModPhys.80.633](https://doi.org/10.1103/RevModPhys.80.633)

Nussbaumer, H., Schmid, H. M., & Vogel, M. 1989, A&A, 211, L27

O'Dell, C. R., & Yusef-Zadeh, F. 2000, AJ, 120, 382, doi: [10.1086/301429](https://doi.org/10.1086/301429)

Osterbrock, D. E., & Ferland, G. J. 2006, Astrophysics of gaseous nebulae and active galactic nuclei, 2nd edn. (Sausalito, CA: University Science Books)

Salgado, F., Berné, O., Adams, J. D., et al. 2016, ApJ, 830, 118, doi: [10.3847/0004-637X/830/2/118](https://doi.org/10.3847/0004-637X/830/2/118)

Schmid, H. M. 1989, A&A, 211, L31

Stoerzer, H., & Hollenbach, D. 1998, ApJ, 495, 853, doi: [10.1086/305315](https://doi.org/10.1086/305315)

Stoerzer, H., Stutzki, J., & Sternberg, A. 1997, A&A, 323, L13

van der Werf, P. P., Goss, W. M., & O'Dell, C. R. 2013, ApJ, 762, 101, doi: [10.1088/0004-637X/762/2/101](https://doi.org/10.1088/0004-637X/762/2/101)

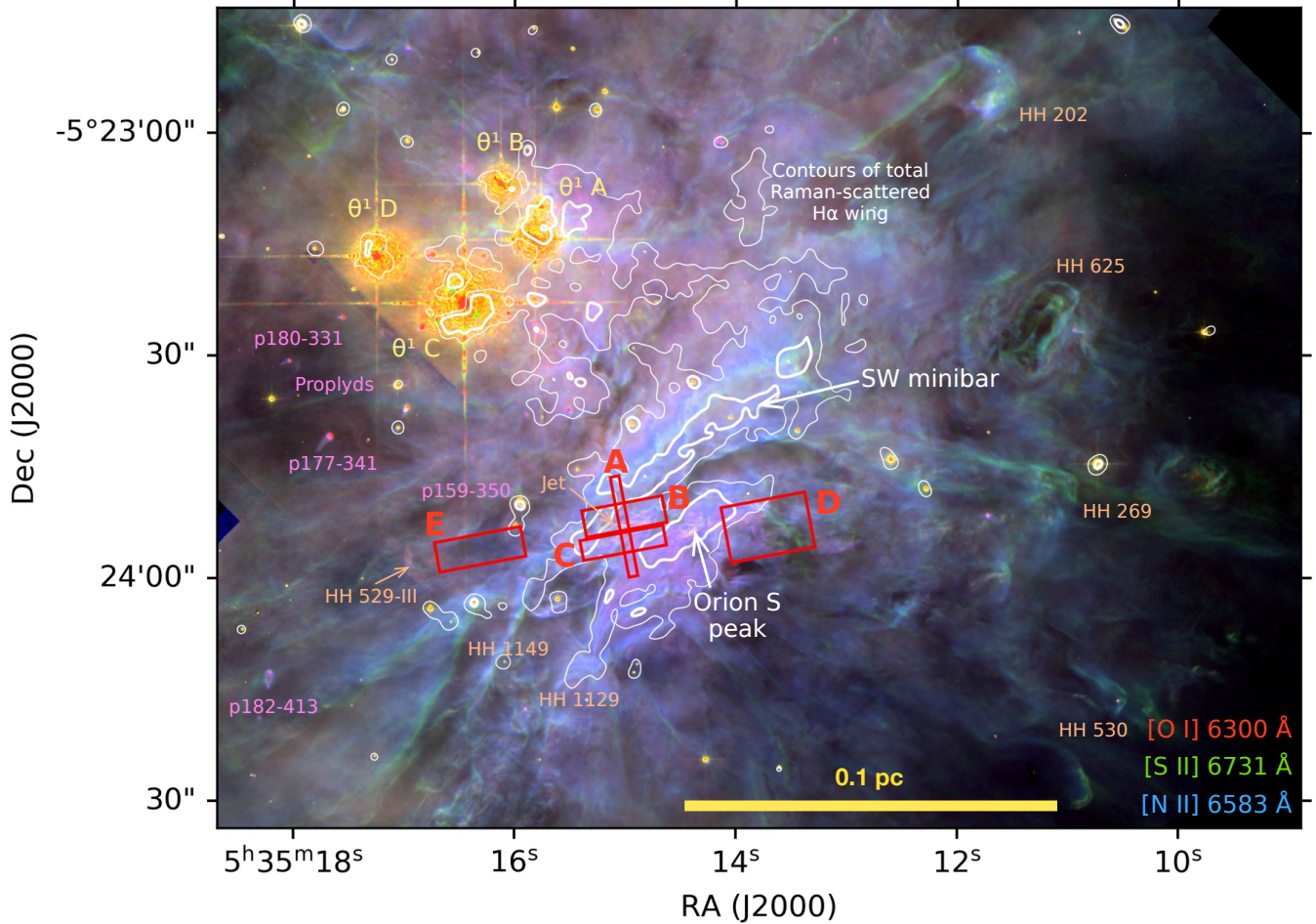


**Figure 6.** Zoom on Trapezium and Orion South region, showing regions of extracted Keck spectra.

Van Hoof, P. A. M. 2018, Galaxies, 6,

Watson, A. M., Henney, W. J., & Escalante, V. 1998, in American Astronomical Society Meeting Abstracts, Vol. 193, 16.03

doi: [10.3390/galaxies6020063](https://doi.org/10.3390/galaxies6020063)

Weilbacher, P. M., Monreal-Ibero, A., Kollatschny, W., et al. 2015, A&A, 582, A114, doi: [10.1051/0004-6361/201526529](https://doi.org/10.1051/0004-6361/201526529)

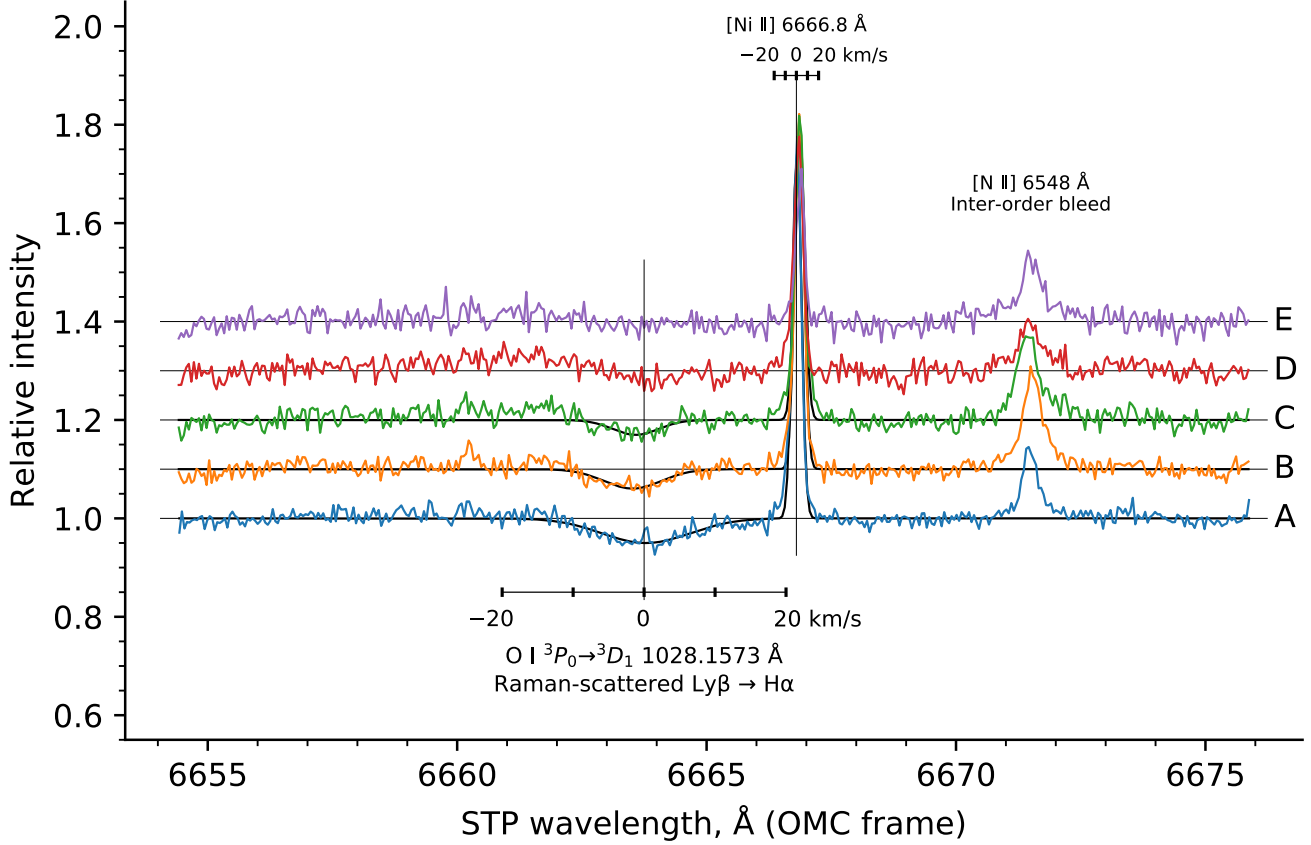


**Figure 7.** Keck HIRES spectra of Raman-scattered O I absorption line for five regions in Orion South. Wavelengths are given on an air scale and in the rest-frame of the Orion Molecular Cloud, as defined by the peak velocity of  $^{13}\text{CO}$ .

## APPENDIX

### A. REANALYSIS OF 21 CM H I OBSERVATIONS OF THE ORION BAR

Karl G. Jansky Very Large Array observations of the H I 21 cm line from the Orion Nebula and its surroundings at a spatial resolution of  $\approx 6''$  and a velocity resolution of  $0.77 \text{ km s}^{-1}$  were presented in van der Werf et al. (2013, hereafter vdW13). The line is seen both in emission and absorption of the strong free-free continuum emitted by the ionized nebula. The majority of the absorption arises in the foreground Veil at Local Standard of Rest velocities of  $v_{\text{lsr}} = -2 \text{ km s}^{-1}$  to  $+7 \text{ km s}^{-1}$ . Emission is seen primarily at more redshifted velocities of  $+10 \text{ km s}^{-1}$  to  $+15 \text{ km s}^{-1}$ , similar to the velocities of the molecular gas seen in CO, although at large distances from the center of the nebula the Veil is also seen in emission. The analysis of the absorption components by vdW13 was carried out under the assumptions that (i) all of the continuum emission arises from *behind* the absorbing H $^0$  column (from the point of view of the Earth), and (ii) line emission is negligible at velocities where absorption is detected. These are both very good assumptions in the case of absorption by the foreground Veil, but they break down for the case of the Orion Bar, where both emission and absorption are seen at similar velocities and in spatially adjacent regions. Given the wealth of information on the physical conditions and geometry that these data provide, it is worth reanalyzing them under less restrictive assumptions.

In the Rayleigh–Jeans limit, the frequency-dependent surface brightness  $I_\nu$  is characterized by the brightness temperature in each velocity channel:  $T_b(v) = c^2 I_\nu / 2k\nu^2$ , where  $v/c = (\nu/\nu_0) - 1$  and  $\nu_0 = 1.420\,405 \text{ GHz}$ . The radiative transfer equation can be solved for an idealized three-layer sandwich structure (see Fig. 14), consisting of (1) a background H $^+$  region with electron temperature  $T_e$  and free-free continuum optical depth  $\tau'$ , (2) an intermediate neutral H $^0$  layer with spin temperature  $T_s$  and line

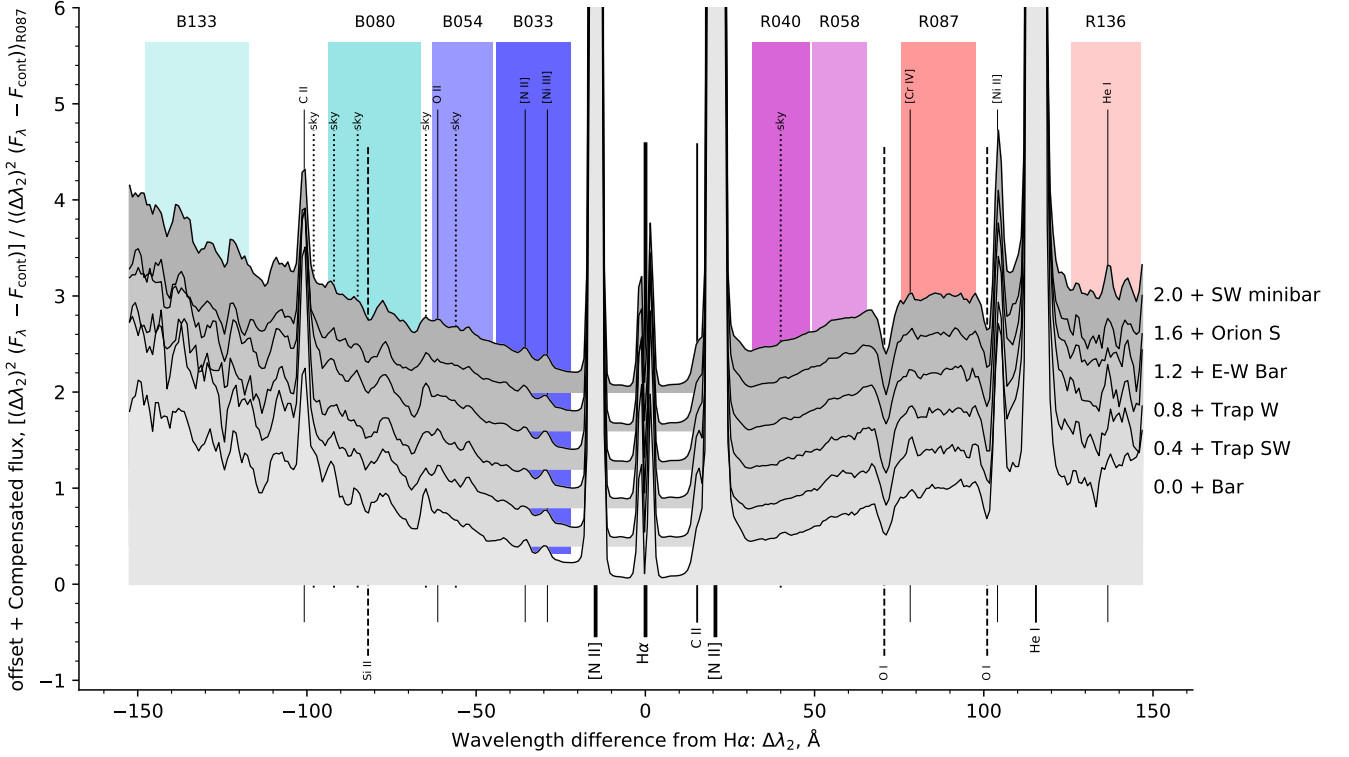


**Figure 8.** Same as Fig. 3 but with  $F_\lambda$  multiplied by  $(\Delta\lambda_2)^2$  and zoomed in on the Raman wing wavelengths. The spectrum is normalized by the average flux in the R087 band and each region is offset vertically by a constant value, as indicated at right. In this presentation, optically thin Raman scattering of a flat FUV spectrum should give a constant value, which for the Orion data is only seen in the R087 and R136 bands.

optical depth  $\tau(v)$ , and (3) a foreground  $H^+$  region with the electron temperature  $T_e$  and free-free continuum optical depth  $\tau''$ . The continuum source function in regions 1 and 3 is  $T_e$ , whereas the line source function in region 2 is  $T_s$ . Region 2 is assumed to have zero continuum optical depth. Following vdW13, large-scale Milky Way  $H\alpha$  line emission along the line of sight through Orion is neglected since it is (a) very faint compared with the nebula, with  $T_b(v) < 48$  K at  $v = 10 \text{ km s}^{-1}$  (Green 1991; Green & Padman 1993), and (b) any emission that is smooth on angular scales below 7 arcminutes will be filtered out by the interferometer.

At continuum frequencies just off the line,  $\tau(v) = 0$  and only regions 1 and 3 contribute to the observed brightness, yielding a continuum brightness temperature

$$\begin{aligned} T_c &= T_e \left( 1 - e^{-(\tau' + \tau'')} \right) \\ &= T_c' e^{-\tau'} + T_c'', \end{aligned} \quad (\text{A1})$$

where the second equality gives the decomposition into separate contributions from region 1:  $T_c' = T_e(1 - e^{-\tau'})$ , and region 3:  $T_c'' = T_e(1 - e^{-\tau''})$ . At frequencies where the line opacity is significant, all three regions contribute, yielding

$$T_b(v) = T_c' e^{-(\tau(v) + \tau'')} + T_s \left( 1 - e^{-\tau(v)} \right) e^{-\tau''} + T_c''. \quad (\text{A2})$$

For practical reasons related to the deconvolution of the interferometric data, the results of vdW13 are presented in continuum-free form as  $\tilde{T}_b(v) = T_b(v) - T_c$ . Combining equation (A1) and (A2), one finds

$$\tilde{T}_b(v) = \left[ 1 - e^{-\tau(v)} \right] \left[ 1 - (T_c''/T_e) \right] \left[ T_s - T_c' \right]. \quad (\text{A3})$$

The relative brightness temperature of the line,  $\tilde{T}_b(v)$ , is therefore seen to be the product of three factors, given by the three sets of square brackets in equation (A3). The first two factors are always positive since  $\tau(v) \geq 0$  and  $T_c'' \leq T_e$ , but the third factor

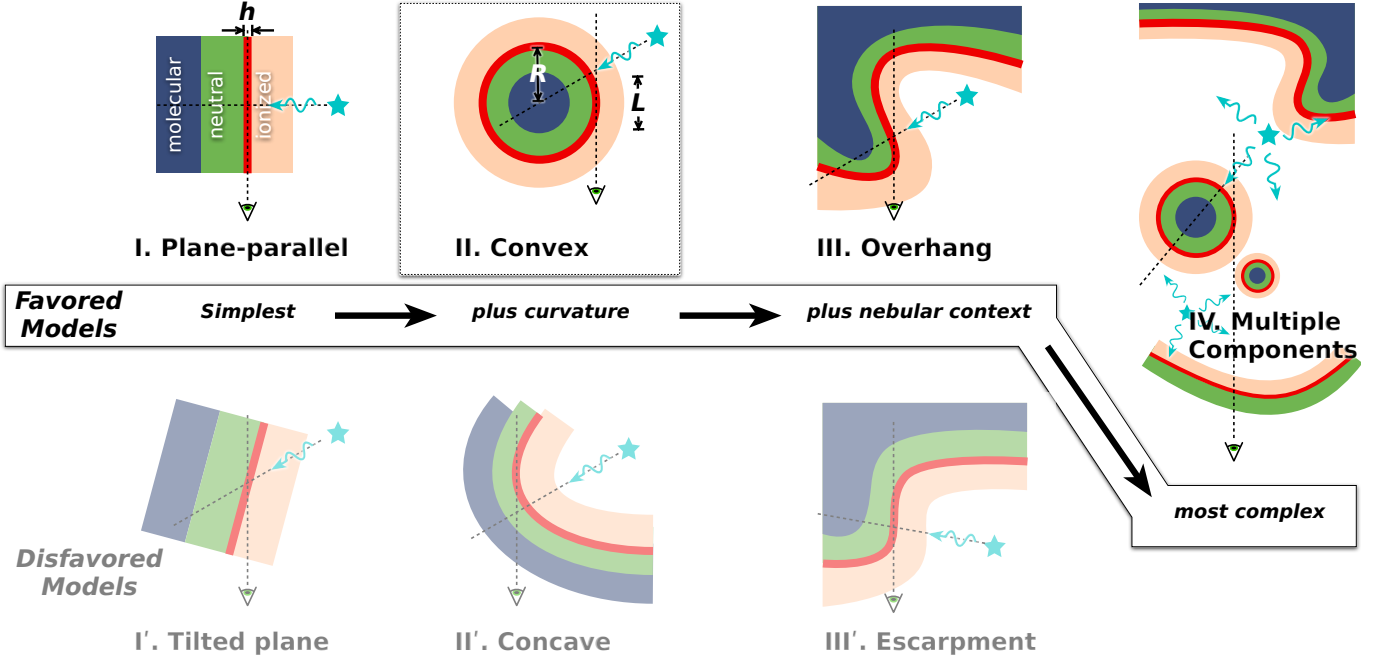


**Figure 9.** Different classes of geometrical models that have been proposed for the Orion Bar. The sequence of models I, II, III, IV are of increasing complexity, but also increasing scope and explanatory power. Models I', II', III', on the other hand, are disfavored due to either underperformance or falsification (see text for further details). For all models, dark blue shading represents molecular gas, green shading represents neutral gas, and light orange shading represents ionized gas. An example emission layer of thickness  $h$  and radius of curvature  $R$  is indicated by thick red lines. The line-of-sight depth of the emission layer is denoted by  $L$ . The direction of illumination and the line of sight are indicated by thin dotted lines.

can take either sign. When the continuum brightness temperature  $T_c'$  of the background photoionized gas in region 1 exceeds the spin temperature  $T_s$  of neutral hydrogen in region 2, then we see an absorption line:  $\tilde{T}_b(v) < 0$ . On the other hand, when  $T_s$  is higher than  $T_c'$ , then we see an emission line:  $\tilde{T}_b(v) > 0$ . In either case, the maximum line strength will be found when region 2 is opaque ( $\tau(v) \gg 1$ ) and region 3 is transparent ( $T_c'' \ll T_e$ ), yielding  $\max(|\tilde{T}_b(v)|) = |T_s - T_c'|$ .

The electron temperature in the ionized gas is expected to be roughly constant at  $T_e \approx 11\,000$  K (Dicker et al. 2009), but this still leaves 4 unknown quantities,  $\tau(v)$ ,  $T_s$ ,  $T_c'$ , and  $T_c''$ , to be determined from 2 observed quantities:  $T_c$  and  $\tilde{T}_b(v)$ . Further assumptions must therefore be made in order to interpret the observations, but these can be guided by the observed spatial trends and simple geometric models. For instance, in the Orion Bar the free-free continuum brightness temperature falls sharply across the ionization front from  $T_c \approx 3000$  K on the ionized side, but then levels off to a roughly constant value of  $T_c \approx 600$  K on the neutral side. Assuming that this constant value reflects unrelated foreground emission (probably ionized by  $\theta^2$  Ori A) that overlays the entire Bar (this hypothesis is tested below), we have an upper limit to the background emission of  $T_c - 600$  K. It can be further assumed that the emission from region 1 is a constant fraction,  $f_{bg}$ , of this upper limit:

$$T_c' = f_{bg}(T_c - 600 \text{ K}) . \quad (\text{A4})$$

If the Bar geometry is a cylinder that is illuminated from the side (see Fig. XXX), then  $f_{bg} = 0.5$  is appropriate. If the Bar is illuminated from slightly behind, or if it is an escarpment, or if an additional background component is present (see § 5.1), then the fraction will be larger:  $0.5 < f_{bg} < 1.0$ .

Further progress can then be made by considering null points in the nebula where line emission and absorption cancel out. At such points  $\tilde{T}_b(v) \approx 0$ , so that  $T_s = T_c'$  by equation (A3). Absorption component M is identified by vdW13 as associated with H $^0$  in the Bar, due to its velocity and spatial distribution. Component M consists of a string of knots with  $\tilde{T}_b(v) = -200$  to  $-400$  K at  $v \approx 11 \text{ km s}^{-1}$ . They are arranged parallel to the Bar, just behind the ionization front at a relative position of roughly +0.006 pc (see Fig. 5) and where the continuum brightness has fallen to  $T_c \approx 2200$  K. At greater distances from the ionization front the H $1$  at this velocity is seen in emission, reaching a peak of  $\tilde{T}_b(v) \approx +250$  K at +0.030 pc where  $T_c \approx 750$  K. The crossover null point where  $\tilde{T}_b(v) = 0$  occurs between these two at +0.012 pc where  $T_c \approx 1500$  K.

Add a table showing

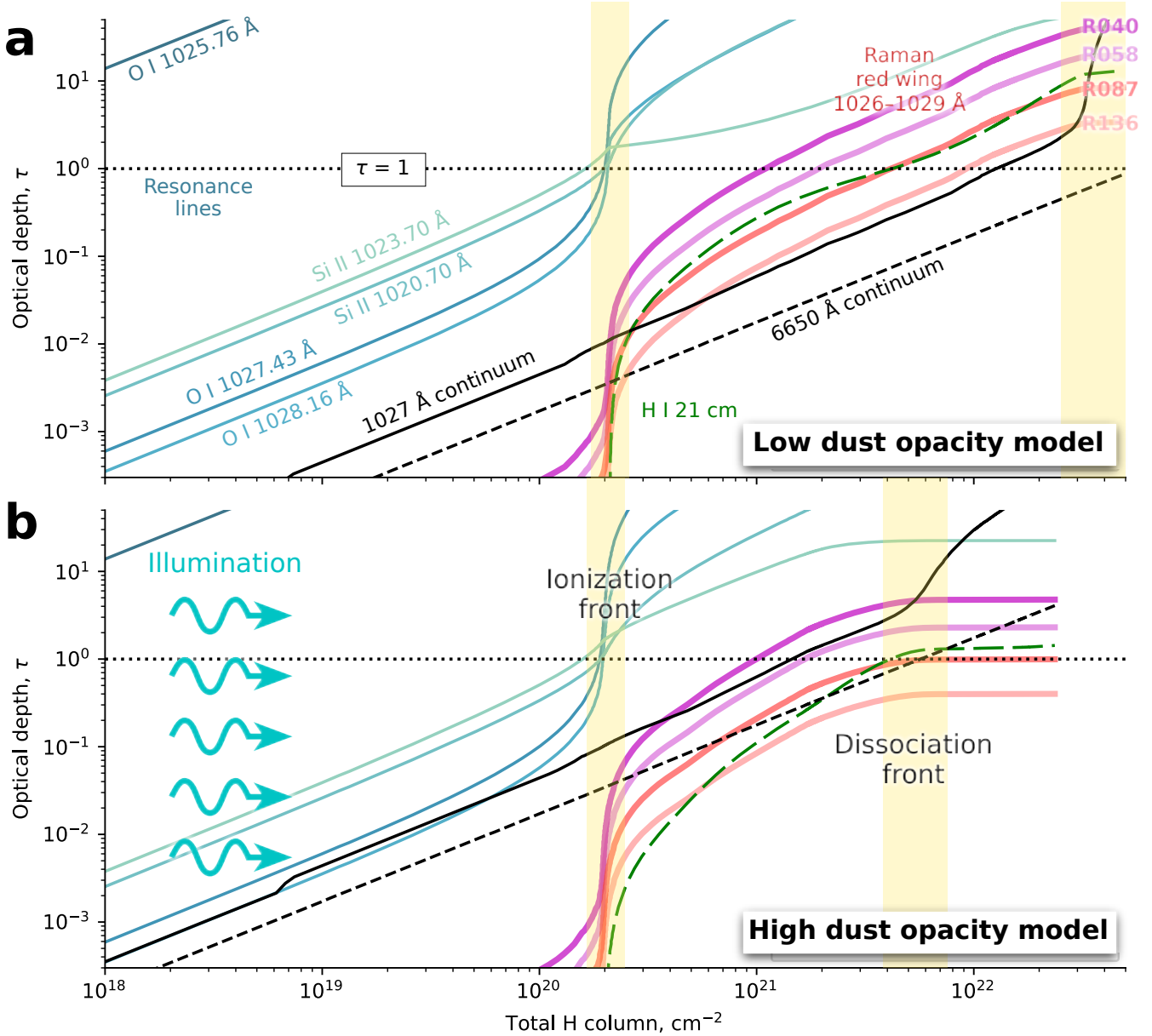


**Figure 10.** Optical depth of select processes as a function of total hydrogen nucleon column density, calculated from static Cloudy simulations of the Orion Bar. All optical depths and columns are measured with respect to the illuminating Trapezium stars, which are situated to the left in this figure. Separate panels show two models that differ only in the assumed dust absorption opacity: (a) low opacity,  $\sigma_{\text{FUV}} \approx 5 \times 10^{-23} \text{ cm}^2 \text{ H}^{-1}$ , and (b) high opacity,  $\sigma_{\text{FUV}} \approx 5 \times 10^{-22} \text{ cm}^2 \text{ H}^{-1}$ . Optical depths of  $O^0$  and  $Si^+$  absorption lines in the Ly $\beta$  wings are shown in blue. Continuum optical depths near Ly $\beta$  (solid line) and H $\alpha$  (dashed line) are shown in black. The H $^0$  21 cm line optical depth is shown in green (long dashed line). Optical depths to Rayleigh/Raman scattering for 4 observed bands in the red wing of Ly $\beta$  (see Table 2) are shown in red.

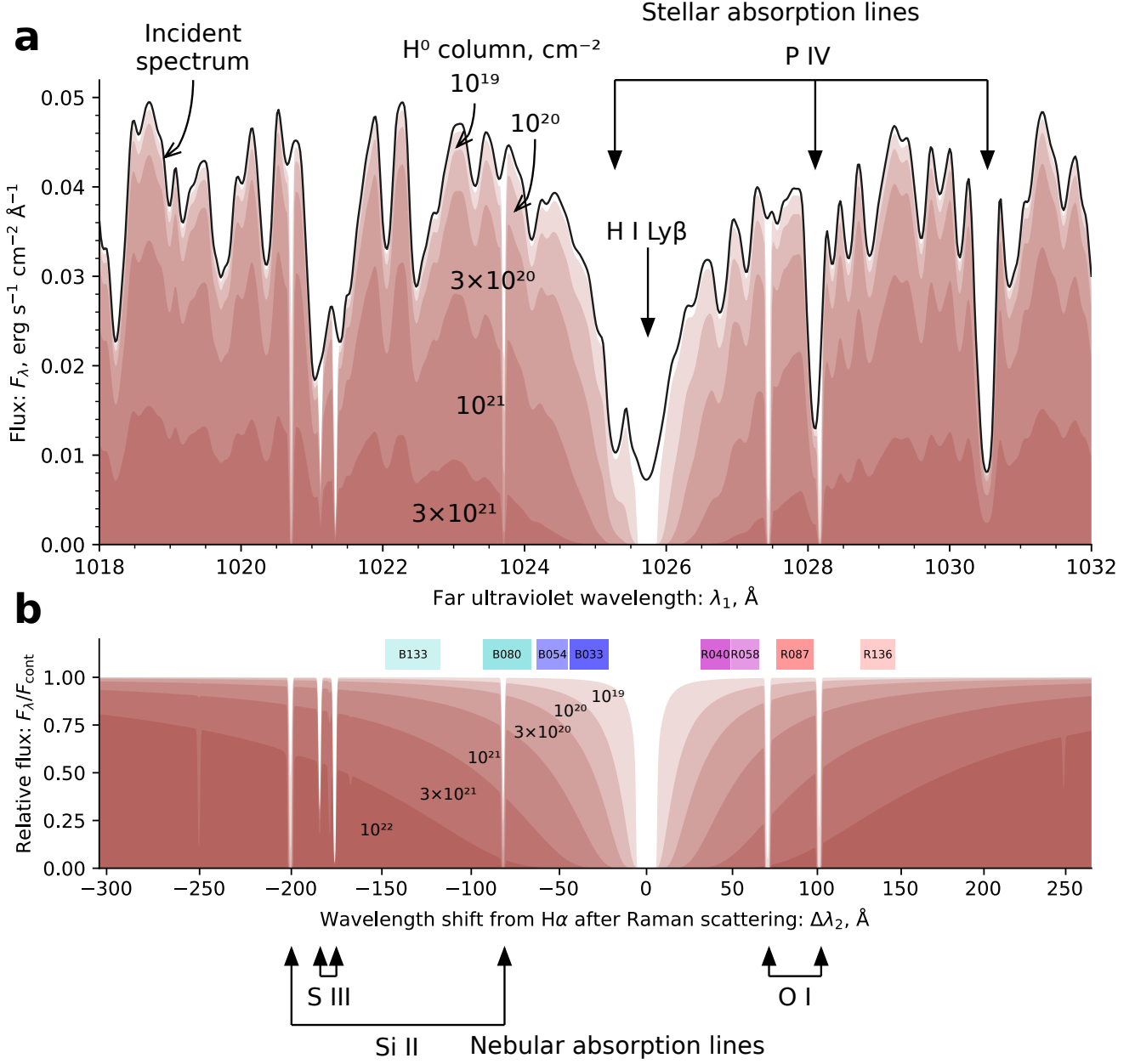


**Figure 11.** (a) Predicted spectrum of Trapezium stars in vicinity of Ly $\beta$  from POWR OB atmosphere models (black line), together with attenuation by Cloudy model of the Orion Bar (red filled shapes), extracted at a series of values of the neutral hydrogen column density, as marked. (b) Relative attenuation of the incident spectrum by line opacity only (that is, neglecting dust continuum opacity) in the Cloudy models, which shows the development of the Ly $\beta$  damping wings as the column density increases. In this panel, the  $x$  axis is labelled with  $\Delta\lambda_2$  in the optical domain, allowing direct comparison with the observations presented in Figure 8 (observed Raman bands are indicated by colored boxes). Note that the scale is linear in  $\lambda_1$ , which is slightly non-linear in  $\Delta\lambda_2$ . Wavelengths of some of the more prominent stellar photospheric lines and nebular absorption lines are marked.

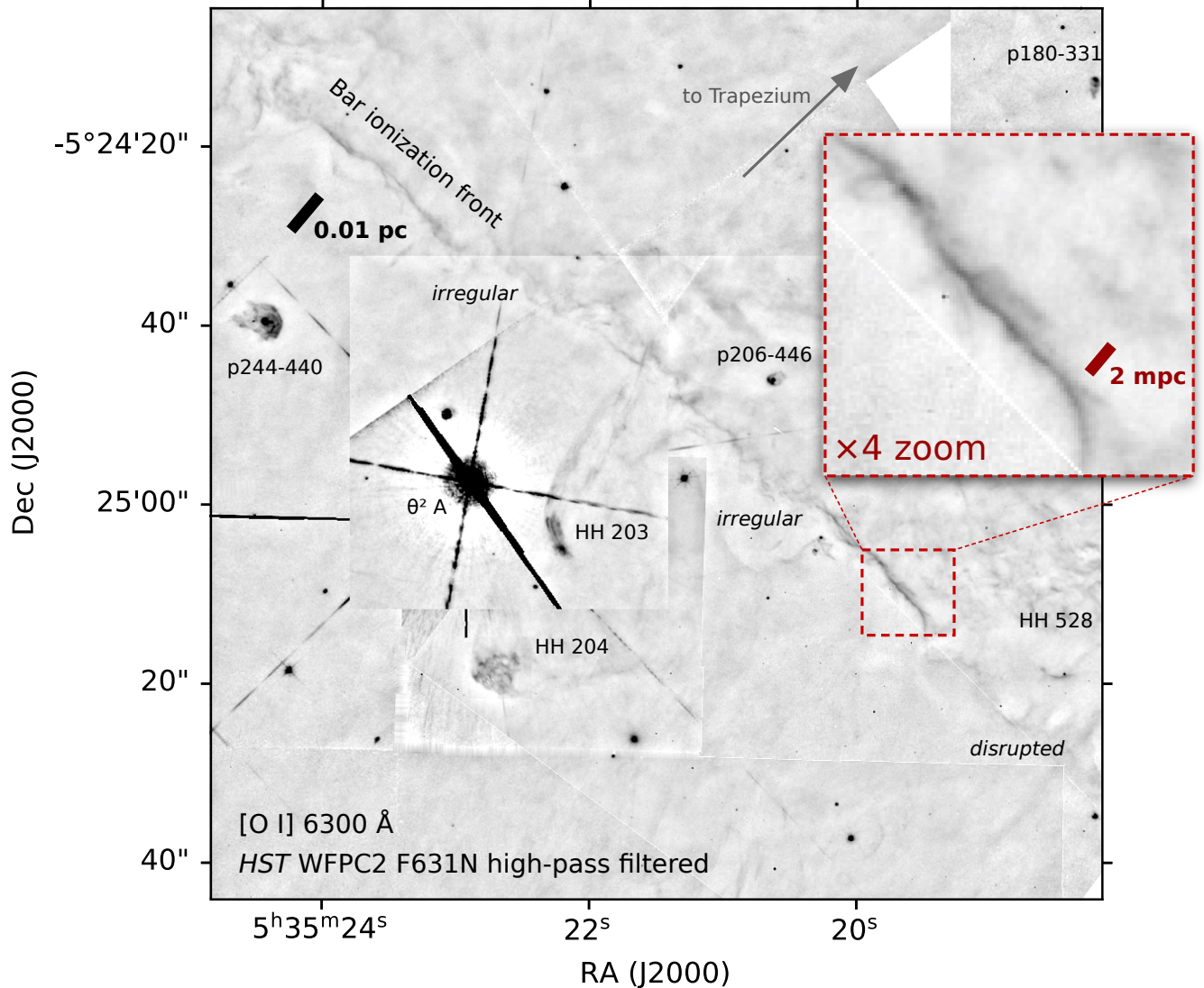


**Figure 12.** Fine-scale structure of the ionization front at the Orion Bar.

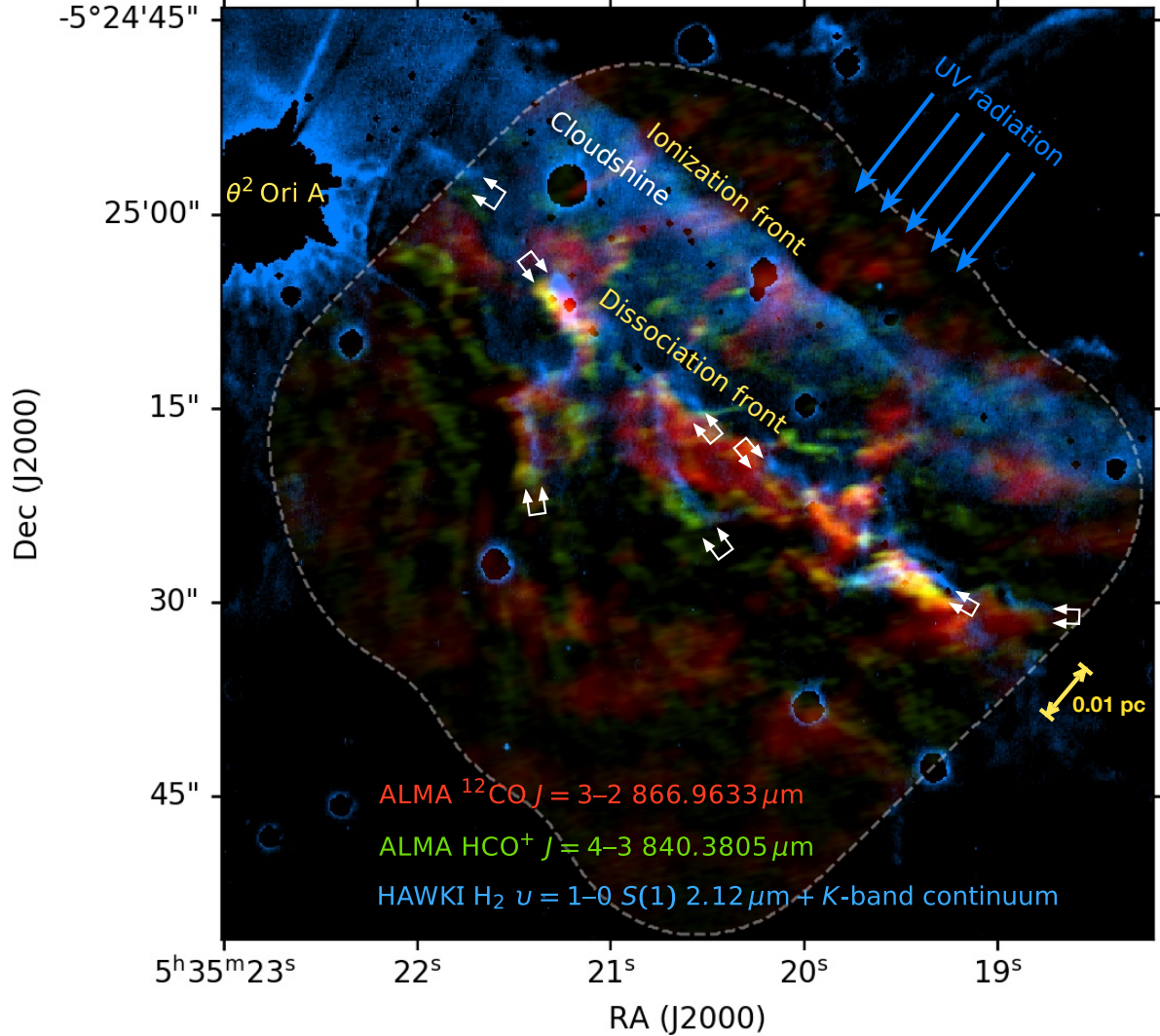


**Figure 13.** Fine-scale structure of the dissociation front in the Orion Bar. Double white arrows mark out some instances of stratification between emission of H<sub>2</sub> (blue) and heavier molecules (green/yellow/red). In every instance H<sub>2</sub> is displaced towards the irradiated side of the filament by 1'' to 2'' ( $\approx 0.003$  pc). Background image shows ALMA mosaics (Goicoechea et al. 2016) of the sub-mm CO  $J = 3 \rightarrow 2$  866.96  $\mu\text{m}$  HCO<sup>+</sup> 840.38  $\mu\text{m}$  emission lines in the red and green color channels, respectively, with the boundary of the ALMA field shown by the gray dashed line. The blue color channel of the background image shows near-infrared vibrationally excited H<sub>2</sub>  $v = 1 \rightarrow 0$  S(1) 2.12  $\mu\text{m}$  emission, extracted from narrow-band imaging with ESO's High Acuity Wide-field Imager (HAWK-I, Kissler-Patig et al. 2008). The H<sub>2</sub> image has been corrected for contamination by ionized emission (mainly hydrogen Brγ recombination line), but has not been continuum-subtracted. As a result, scattered starlight (cloudshine, Foster & Goodman 2006) is seen as a band of diffuse emission that falls off smoothly behind the ionization front.

**Figure 14.** Three-layer sandwich structure for H I 21 cm radiative transfer.